Coupled Systems Mechanics, *Vol. 14, No. 5 (2025) 489-505*
https://doi.org/10.12989/csm.2025.14.5.489

Dynamic response of graphene-platelets reinforced circular plates subjected to low-velocity impact with spinning motion

Nannan Zhang[1], Wubin Shan*[1], Qiong Shi[1] and Huan Li[2]

[1]*School of Elevator Engineering, Hunan Electrical College of Technology, 411101, Xiangtan, PR China*
[2]*Changsha Environmental Protection College, Changsha, 410004, PR China*

(Received August 22, 2025, Revised October 19, 2025, Accepted October 31, 2025)

Abstract. This study pioneers the analysis of low-velocity impact behavior in spinning functionally graded porous circular plates reinforced with graphene platelets (GPLs), employing first-order shear deformation theory. The governing equations are derived via Hamilton's principle, while the plate-impactor interaction is modeled using a modified Hertzian contact law. Numerical solutions are validated against existing literature showing excellent agreement. Parametric studies investigate the effects of:(1) Spinning speed (revealing that higher speeds increase contact force but reduce impact displacement), (2) Porosity characteristics (distribution patterns and coefficients), (3) GPL reinforcement configurations, and (4) Nanofiller weight fractions on the dynamic response. Results highlight that porosity distribution has the most pronounced influence on both contact force evolution and transient center-point deflection, outweighing other variables.

Keywords: circular plate; graphene platelets; low-velocity impact; metal foam; spinning motion

1. Introduction

Low-velocity impact is critically important in engineering safety. It involves the damage initiation, propagation, and failure mechanisms of materials/structures under low-speed collisions, directly affecting safety in key sectors like aerospace and transportation (Song *et al.* 2019, Yang *et al.* 2022, Fan and She 2026, Fan *et al.* 2025a, 2025b). Statistics indicate approximately 15% of mechanism-related accidents stem from cumulative low-velocity impact damage. Research in this area optimizes impact-resistant designs, extends equipment lifespan, and reduces maintenance costs. Current studies focus on predicting the dynamic response of composite materials and innovating protective structures, holding profound implications for ensuring personnel safety and structural integrity. Furthermore, research articles specifically on low-velocity impact on circular plates are very limited, particularly within this existing literature. This overview summarizes key research on the low-velocity impact (LVI) behavior of composite circular plates: Khatounabadi *et al.* (2025) utilized a modified Hertzian contact law and finite element method (FEM) to analyze LVI on porous circular plates reinforced with graphene platelets. Raissi (2021) investigated the

*Corresponding author, Professor, E-mail: shanwubin2020@163.com

http://www.techno-press.org/?journal=csm&subpage=8 ISSN: 2234-2184 (Print), 2234-2192 (Online)

dynamic response of composite plates impacted by a cylindrical striker with an initial velocity of 1 m/s. Mars *et al.* (2018) pioneered the LVI analysis of elastoplastic functionally graded material (FGM) plates. Their approach integrated the Mori-Tanaka model for micromechanical property determination and Suquet's self-consistent method for stress-field homogenization. Gunes *et al.* (2014) explored the LVI behavior of clamped functionally graded circular plates through combined experimental testing and explicit finite element modeling. Shariyat and Jafari (2013a) developed a weighted residual semi-analytical solution with an iterative scheme to analyze LVI on functionally graded plates, highlighting limitations of the simple rule of mixtures. Dai *et al.* (2013) studied the nonlinear dynamic response of functionally graded circular plates subjected to LVI, employing Giannakopoulos' contact model to derive expressions for contact force and central deflection. Shariyat and Jafari (2013b) presented a Galerkin-type solution procedure for the nonlinear LVI analysis of circular plates with bidirectional material gradation under radial preloads. Gunes *et al.* (2011) conducted a three-dimensional elastoplastic analysis of functionally graded (SiC/Al) circular plates experiencing low-velocity impact loads.

While rotational motion is frequently neglected in contemporary circular plate vibration studies, its influence necessitates consideration. Recent research addressing this gap includes: Mirdrikvandi *et al.* (2025) applied the differential quadrature method to examine free vibration in rotating sandwich annular plates featuring porous cores and carbon nanotube-reinforced polymeric nanocomposite face sheets. Morozov *et al.* (2024) developed a model for the coupled plane-transverse vibrations of rotating thin circular plates with concentric holes, explicitly incorporating Coriolis and centrifugal inertial forces generated by in-plane rotation. Li and Hu (2021) explored principal and 3:1 internal resonances in rotating, edge-clamped conductive circular plates within an air-magnetic field, identifying period-doubling bifurcations in intermittent periodic responses. Hu and Li (2019) investigated magnetoelastic axisymmetric multi-mode interactions and Hopf bifurcations in conductive circular plates rotating through air and transverse magnetic fields using multiple scales combined with polar coordinate transformation. Yang *et al.* (2019) studied the thermoelastic coupling effects on vibration and stability in rotating friction circular plates, incorporating middle internal forces and deformation effects. Hu and Li (2018) characterized primary resonance and bifurcation phenomena in rotating conductive plates subjected to air-magnetic fields, employing bifurcation diagrams, maximum Lyapunov exponents, and parametric response analysis. Hu *et al.* (2018) examined nonlinear magneto-elastic combined resonances (parametric and forced) in circular plates rotating with variable speed under alternating load, based on derived magneto-elastic vibration equations. Hu and Wang (2016) focused on the nonlinear free vibration of conductive rotating thin circular plates under static loads within a magnetic field, deriving the governing nonlinear equations of motion. Hu and Wang (2015) utilized a modified multiple scale method to determine amplitude-frequency characteristics and relationships between amplitude, static loads, and excitation forces for the plate. Younesian *et al.* (2015) presented analytical closed-form solutions (series expansions) for deflection, strain, and stress distributions in hollow circular plates subjected to a rotating peripheral force. Li *et al.* (2011) derived dynamic governing equations and boundary conditions for rotating laminated circular plates with viscoelastic core layers using Hamilton's principle. Bui *et al.* (2024) investigated the thermo-mechanical dynamic buckling and vibration of FG-GPLRC circular plates and shallow spherical shells on nonlinear viscoelastic foundations. Nam *et al.* (2025) developed a semi-analytical method for analyzing the nonlinear dynamic responses of functionally graded porous graphene platelet-reinforced circular plates and spherical shells. Nguyen *et al.* (2024) examined the thermo-mechanical axisymmetric stability of FG-GPLRC spherical shells and circular plates on nonlinear

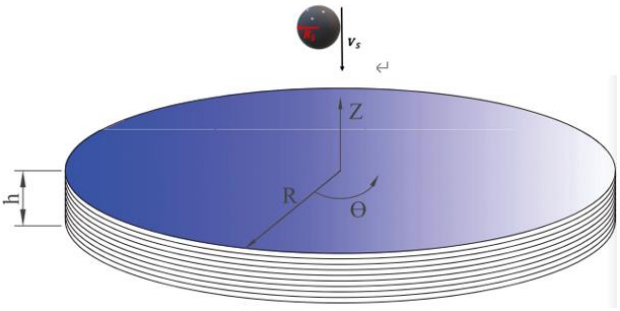

(a) The sketch of the circular plate

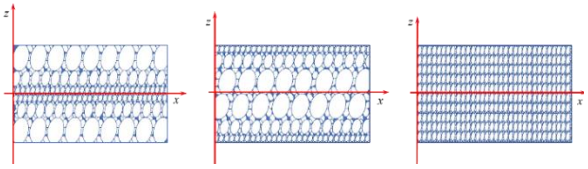

(b) Porosity-I, Porosity-II, Porosity-III

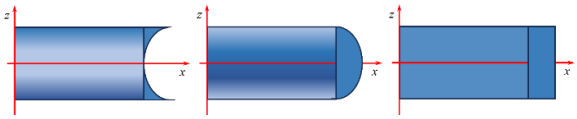

(c) GPL-X, GPL-O, GPL-UD

Fig. 1 The sketch of low-velocity impact response of graphene-reinforced porous circular plates

elastic media. Meanwhile, Vu *et al.* (2025a) studied the vibration responses of graphene platelet-reinforced circular plates and spherical shells with multi-step spiderweb stiffeners and piezoelectric layers. In another work, Vu *et al.* (2025b) proposed a semi-analytical approach for analyzing the nonlinear electro-thermo-mechanical dynamic responses of FG-GPLRC shallow spherical caps and circular plates with porous cores.

The preceding literature review reveals that existing research on the dynamic analysis of rotating circular plates focuses primarily on resonant vibrations (free and forced), with relatively few dedicated studies (Hu and Ma 2019, Li *et al.* 2017). Crucially, no prior investigation addresses the low-velocity response of these structures subjected to low-velocity impact loads considering the effect of spinning motion. To address this gap, this study pioneers the exploration of this specific low-velocity regime. The objectives of this paper is to develop a mathematical model for the rotating circular plate under low-velocity impact loads, incorporating three distinct material distribution patterns and accounting for rotational dynamics, and implement a computational framework based on the finite difference method combined with an iterative technique to solve the resulting nonlinear low-velocity dynamic equations, and conduct numerical simulations to demonstrate the influence of key parameters on the impact force history and the plate's temporal response.

2. Theoretical modeling

Fig. 1 shows the circular plate, having thickness h and radius R. The displacement components

u, *v*, and *w* correspond to the mid-plane directions *r*, θ, and *z* within the cylindrical coordinate system centered there. Three porosity distributions across the plate's thickness are defined in Fig. 2. This study considers three distinct porosity distributions through the thickness (*z*-axis) of the circular plate: a uniform distribution (Porosity-III) and two non-uniform symmetric distributions (Porosity-I and Porosity-II). The corresponding variations in material properties along the z-axis are as follows (Zhou *et al.* 2024, Kalhori *et al.* 2023a, 2023b, Caglar *et al.* 2025, Shen *et al.* 2024, Wang *et al.* 2023, Wu *et al.* 2023, Xia *et al.* 2023, Zhao *et al.* 2024a, 2024b, Cheng *et al.* 2025, Cheng and She 2025, Ma *et al.* 2025, She and He 2025),

For Porosity-I

$$\begin{aligned} E(z) &= E^*\left[1-e_1\left\{1-\cos(\frac{\pi z}{h})\right\}\right], \\ \rho(z) &= \rho^*\left[1-e_{m1}\left\{1-\cos(\frac{\pi z}{h})\right\}\right], \\ \mu(z) &= \mu^*. \end{aligned} \tag{1}$$

For Porosity-II

$$\begin{aligned} E(z) &= E^*\left[1-e_2\cos(\frac{\pi z}{h})\right], \\ \rho(z) &= \rho^*\left[1-e_{m2}\cos(\frac{\pi z}{h})\right], \\ \mu(z) &= \mu^*. \end{aligned} \tag{2}$$

For Porosity-III

$$E(z) = E^* e_3, \quad \rho(z) = \rho^* e_{m3}, \quad \mu(z) = \mu^*. \tag{3}$$

Herein, the plate's position-dependent material properties are defined as: elastic modulus $E(z)$, mass density $\rho(z)$, Poisson's ratio $\mu(z)$; Mass density coefficients are denoted e_{m1}, e_{m2}, e_{m3}; while porosity size parameters are e_1, e_2, e_3; and the relationship between e_{mi} and e_i are as follows (Zhang *et al.* 2024)

$$\begin{cases} 1-e_{m1}\left\{1-\cos(\frac{\pi z}{h})\right\} = \sqrt{1-e_1\left\{1-\cos(\frac{\pi z}{h})\right\}}, \text{(GPL-X)} \\ 1-e_{m2}\cos(\frac{\pi z}{h}) = \sqrt{1-e_2\cos(\frac{\pi z}{h})}, \text{(GPL-O)} \\ e_{m3} = \sqrt{e_3}, \text{(GPL-UD)} \end{cases} \tag{4}$$

To comparatively assess various porosity and GPL distribution patterns, all plate configurations are constrained to maintain identical total mass across different porosity-GPL combinations. This yields (Nam *et al.* 2025)

$$\int_0^{\frac{h}{2}} \sqrt{1-e_1\left\{1-\cos(\frac{\pi z}{h})\right\}}dz = \int_0^{\frac{h}{2}} \sqrt{1-e_2\cos(\frac{\pi z}{h})}dz = \int_0^{\frac{h}{2}} \sqrt{e_3}dz \tag{5}$$

Where e_1 (a given input) defines the porosity coefficients e_2 and e_3. And, these non-porous material properties (E^*, μ^*, ρ^*, α^*) have the following form (Jafary *et al.* 2025)

$$E^* = E_m\left(\frac{3}{8}\left(\frac{1+\zeta_L\eta_L V_{GPL}}{1-\eta_L V_L}\right)+\frac{5}{8}\left(\frac{1+\zeta_W\eta_W V_{GPL}}{1-\eta_L V_{GPL}}\right)\right), \tag{6}$$

$$\begin{aligned}\rho^* &= \rho_{GPL}V_{GPL}+\rho_m V_m,\\ \mu^* &= \mu_{GPL}V_{GPL}+\mu_m V_m.\end{aligned} \tag{7}$$

Herein, E_{GPL} and E_m stand for Young's modulus of GPLs and matrix. The same subscript notation applies to Poisson's ratio ν_{GPL} (ν_{m}), and mass density ρ_{m} (ρ_{GPL}), and $\zeta_L=\frac{2L_{GPL}}{t_{GPL}}$, $\zeta_W=\frac{2w_{GPL}}{t_{GPL}}$, $\eta_L=\frac{E_{GPL}-E_m}{E_{GPL}+\zeta_L E_m}$, $\eta_W=\frac{E_{GPL}-E_m}{E_{GPL}+\zeta_W E_m}$.

For a transversely deforming circular plate under FSDT, displacements primarily depend on radial coordinate r, angular coordinate θ, and time t. The radial (u_r) and circumferential (u_θ) components respectively describe lengthwise and tangential position changes. The displacement fields take the form (Zhang and Zhou 2025, Abo *et al.* 2025, Lahdiri *et al.* 2024, Kumar *et al.* 2024, Zohra *et al.* 2024, Zhang *et al.* 2023, Li *et al.* 2024)

$$\begin{aligned}u(r,\theta,z,t) &= u_0(r,\theta,t)+z\varphi_r(r,\theta,t),\\ v(r,\theta,z,t) &= v_0(r,\theta,t)+z\varphi_\theta(r,\theta,t),\\ w(r,\theta,t) &= w_0(r,\theta,t)\end{aligned} \tag{8}$$

The midplane displacements along r, θ, and z axes are designated u_0, v_0, and w_0 respectively. Rotational components are denoted ϕ_r (circumferential plane) and ϕ_θ (transverse plane). Under FSDT, selection of an appropriate shear correction factor K_s is critical. However, determination of K_s for composite circular plates remains complex. Thus, we adopt $K_s=\pi^2/12$ throughout this study for simplification (Abo *et al.* 2025, Lahdiri *et al.* 2024, Kumar *et al.* 2024, Zohra *et al.* 2024). Eq. (8) defines the stress-strain relationship as

$$\begin{aligned}\varepsilon_{rr} &= \varepsilon_{rr}^0+z\varepsilon_{rr}^1,\ \varepsilon_{\theta\theta}=\varepsilon_{\theta\theta}^0+z\varepsilon_{\theta\theta}^1,\\ \varsigma_{r\theta} &= \varsigma_{r\theta}^0+z\varsigma_{r\theta}^1,\ \varsigma_{rz}=\varsigma_{rz}^0,\ \varsigma_{\theta z}=\varsigma_{\theta z}^0\end{aligned} \tag{9}$$

with

$$\begin{aligned}\begin{Bmatrix}\varsigma_{rz}^0\\ \varsigma_{\theta z}^0\end{Bmatrix} &= \begin{Bmatrix}\frac{\partial w_0}{\partial r}+\varphi_r\\ \frac{1}{r}\frac{\partial w_0}{\partial\theta}+\varphi_\theta\end{Bmatrix},\ \begin{Bmatrix}\varepsilon_r^1\\ \varepsilon_\theta^1\\ \varsigma_{r\theta}^1\end{Bmatrix}=\begin{Bmatrix}\frac{\partial\varphi_r}{\partial r}\\ \frac{\partial\varphi_\theta}{\partial\theta}\frac{1}{r}+\frac{1}{r}\varphi_r\\ \frac{\partial\varphi_r}{\partial\theta}\frac{1}{r}+\frac{\partial\varphi_\theta}{\partial r}\end{Bmatrix},\\ \begin{Bmatrix}\varepsilon_{rr}^0\\ \varepsilon_{\theta\theta}^0\\ \varsigma_{r\theta}^0\end{Bmatrix} &= \begin{Bmatrix}\frac{\partial u_0}{\partial r}+\frac{1}{2}\left(\frac{\partial w_0}{\partial r}\right)^2\\ \frac{\partial v_0}{\partial\theta}\frac{1}{r}+\frac{1}{2r^2}\left(\frac{\partial w_0}{\partial\theta}\right)^2+\frac{u_0}{r}\\ \frac{\partial v_0}{\partial r}+\frac{\partial u_0}{\partial\theta}\frac{1}{r}+\frac{\partial w_0}{\partial r}\frac{\partial w_0}{\partial\theta}\frac{1}{r}\end{Bmatrix}.\end{aligned} \tag{10}$$

The constitutive relation can be described as

$$\begin{bmatrix}\sigma_{rr}\\ \sigma_{\theta\theta}\\ \sigma_{rz}\\ \sigma_{\theta z}\\ \sigma_{r\theta}\end{bmatrix}=\begin{bmatrix}Q_{11} & Q_{12} & 0 & 0 & 0\\ Q_{12} & Q_{22} & 0 & 0 & 0\\ 0 & 0 & Q_{44} & 0 & 0\\ 0 & 0 & 0 & Q_{55} & 0\\ 0 & 0 & 0 & 0 & Q_{66}\end{bmatrix}\cdot\left\{\begin{bmatrix}\varepsilon_{rr}\\ \varepsilon_{\theta\theta}\\ \varsigma_{rz}\\ \varsigma_{\theta z}\\ \varsigma_{r\theta}\end{bmatrix}\right\} \tag{11}$$

The stiffness coefficients are $Q_{11}=Q_{22}=\frac{E(z)}{1-\mu(z)^2}$, $Q_{12}=\frac{\mu(z)E(z)}{1-\mu(z)^2}$, $Q_{44}=\frac{E(z)}{2[1+\mu(z)]}$, $Q_{55}=Q_{66}=K_s\ Q_{44}$.

Hamilton's principle provides the circular plate governing equations (Hu and Xu 2021)

$$\int_t\left(-\delta U+\delta K-\delta U_r+\delta U_f+\delta W\right)dt=0 \tag{12}$$

The energy terms comprise: U (strain energy), K (kinetic energy), U_r (centrifugally induced potential), U_f (damping virtual strain) and W (impact load work).

$$U_r=\frac{1}{2}\int_{R_b}^{R_a}\int_0^{2\pi}\int_{-h/2}^{h/2}-\rho(z)\Omega^2 u r dz d\theta dr, \tag{13}$$

$$W=-\int_{R_b}^{R_a}\int_0^{2\pi}\left[F_i(t)\delta\left(w_s-w\right)w-c_t\dot{w}\right]r d\theta dr, \tag{14}$$

$$K=\int_{R_b}^{R_a}\int_0^{2\pi}\int_{-h/2}^{h/2}\frac{1}{2}\rho(z)\begin{bmatrix}(\frac{\partial u}{\partial t}-\Omega v)^2\\ +[\frac{\partial v}{\partial t}+\Omega(r+u)]^2\\ +(\frac{\partial w}{\partial t})^2\end{bmatrix}r dz d\theta dr, \tag{15}$$

$$U=\frac{1}{2}\int_{R_b}^{R_a}\int_0^{2\pi}\int_{-h/2}^{h/2}(\sigma_{rr}\varepsilon_{rr}+\sigma_{\theta\theta}\varepsilon_{\theta\theta}+\sigma_{rz}\varsigma_{rz}+K_s\sigma_{\theta z}\varsigma_{\theta z}+K_s\sigma_{r\theta}\varsigma_{r\theta})r dz d\theta dr. \tag{16}$$

Here, Ω is the rotating speed, ct is the damping coefficient, $F_i(t)$ denotes the Hertzian contact force, with separate loading/unloading models per (Gunes *et al.* 2014, 2011)

$$F_i(t)=\begin{cases}\left[\frac{4}{3}\left(\frac{1-\mu_s^2}{E_s}+\frac{1}{E_{11}}\right)^{-1}\sqrt{R_s}\right]\left(w_i-w_s\right)^{3/2}, (\text{loading})\\ F_{\max}\left(\frac{\alpha}{\alpha_{\max}}\right)^{5/2}, (\text{unloading})\end{cases} \tag{17}$$

Definitions: E_{11}: Elasticity modulus (plate' surface), E_s, μ_s: Impactor elasticity modulus and Poisson's ratio, α_{max}: Maximum indentation depth, $F_{\max}$: Maximum impact force, and Ω symbolize rotating velocity. Inserting Eqs. (13)-(16) into Eq. (12) yields

$$\begin{aligned}&\frac{\partial N_{rr}}{\partial r}+\frac{1}{r}\frac{\partial N_{r\theta}}{\partial \theta}+\frac{1}{r}\left(N_{rr}-N_{\theta\theta}\right)+I_0 r\Omega^2\\&=I_0\frac{\partial^2 u_0}{\partial t^2}+I_1\frac{\partial^2 \varphi_r}{\partial t^2}-2I_0\Omega\frac{\partial v_0}{\partial t}-2I_1\Omega\frac{\partial \varphi_\theta}{\partial t},\end{aligned}\tag{18}$$

$$\begin{aligned}&\frac{\partial N_{r\theta}}{\partial r}+\frac{1}{r}\frac{\partial N_{\theta\theta}}{\partial \theta}+\frac{2}{r}N_{r\theta}=I_0\frac{\partial^2 v_0}{\partial t^2}\\&+I_1\frac{\partial^2 \varphi_\theta}{\partial t^2}+2I_0\Omega\frac{\partial u_0}{\partial t}+2I_1\Omega\frac{\partial \varphi_r}{\partial t},\end{aligned}\tag{19}$$

$$\begin{aligned}&\frac{\partial Q_{rr}}{\partial r}+\frac{1}{r}\frac{\partial Q_{\theta\theta}}{\partial \theta}+\frac{Q_{rr}}{r}+\frac{\partial N_{rr}}{\partial r}\frac{\partial w_0}{\partial r}+N_{rr}\frac{\partial^2 w_0}{\partial r^2}\\&+\frac{N_{\theta\theta}}{r^2}\frac{\partial^2 w_0}{\partial \theta^2}+\frac{2N_{r\theta}}{r}\frac{\partial^2 w_0}{\partial r\partial \theta}+\frac{1}{r}\frac{\partial N_{r\theta}}{\partial r}\frac{\partial w_0}{\partial \theta}\\&+\frac{N_{rr}}{r}\frac{\partial w_0}{\partial r}+\frac{1}{r^2}\frac{\partial N_{\theta\theta}}{\partial \theta}\frac{\partial w_0}{\partial \theta}+\frac{1}{r}\frac{\partial N_{r\theta}}{\partial \theta}\frac{\partial w_0}{\partial r}\\&-c_t\frac{\partial w_0}{\partial t}+F_i(t)\delta\left(w_s-w\right)=I_0\left(\frac{\partial^2 w_0}{\partial t^2}-\Omega^2\frac{\partial^2 w_0}{\partial \theta^2}\right),\end{aligned}\tag{20}$$

$$\begin{aligned}&\frac{\partial M_{rr}}{\partial r}+\frac{1}{r}\frac{\partial M_{r\theta}}{\partial \theta}+\frac{1}{r}\left(M_{rr}-M_{\theta\theta}\right)-Q_{rr}+I_1 r\Omega^2\\&=I_1\frac{\partial^2 u_0}{\partial t^2}+I_2\frac{\partial^2 \varphi_r}{\partial t^2}-2I_1\Omega\frac{\partial v_0}{\partial t}-2I_2\Omega\frac{\partial \varphi_\theta}{\partial t},\end{aligned}\tag{21}$$

$$\begin{aligned}&\frac{\partial M_{r\theta}}{\partial r}+\frac{1}{r}\frac{\partial M_{\theta\theta}}{\partial \theta}+\frac{2}{r}M_{r\theta}-Q_{\theta\theta}=\\&I_1\frac{\partial^2 v_0}{\partial t^2}+I_2\frac{\partial^2 \varphi_\theta}{\partial t^2}+2I_1\Omega\frac{\partial u_0}{\partial t}+2I_2\Omega\frac{\partial \varphi_r}{\partial t}.\end{aligned}\tag{22}$$

Herein, $N_{rr}, N_{\theta\theta}, N_{r\theta}, M_{rr}, M_{\theta\theta}, M_{r\theta}, Q_{rz}, Q_{\theta z}$ are defined as follows

$$\begin{aligned}&\begin{bmatrix}N_{rr}\\N_{\theta\theta}\\N_{r\theta}\end{bmatrix}=\int_{-\frac{h}{2}}^{\frac{h}{2}}\begin{bmatrix}\sigma_{rr}\\\sigma_{\theta\theta}\\\sigma_{r\theta}\end{bmatrix}dz,\quad\begin{bmatrix}M_{rr}\\M_{\theta\theta}\\M_{r\theta}\end{bmatrix}=\int_{-\frac{h}{2}}^{\frac{h}{2}}z\cdot\begin{bmatrix}\sigma_{rr}\\\sigma_{\theta\theta}\\\sigma_{r\theta}\end{bmatrix}dz,\\&\begin{bmatrix}Q_{rz}\\Q_{\theta z}\end{bmatrix}=\int_{-\frac{h}{2}}^{\frac{h}{2}}K_s\begin{bmatrix}\sigma_{rz}\\\sigma_{\theta z}\end{bmatrix}dz,\end{aligned}\tag{23}$$

And $\left\{I_0, I_1, I_2\right\}=\int_{-h/2}^{h/2}\rho(z)\left\{1, z, z^2\right\}dz,$

3. Solution method

Closed-form solutions for nonlinear transient responses of rotating circular plates are derived herein via Galerkin discretization. Through assumed mode decomposition of displacement fields, expansions satisfying simply supported ends are formulated

$$\begin{aligned}
\left[u_0,\varphi_r\right] &= \sum_{m=1}^{\infty}\sum_{n=1}^{\infty}\left[U(t),\Phi_r(t)\right]\cos\left(\frac{\pi mr}{R}\right)\sin\left(n\theta\right),\\
\left[v_0,\varphi_\theta\right] &= \sum_{m=1}^{\infty}\sum_{n=1}^{\infty}\left[V(t),\Phi_\theta(t)\right]\sin\left(\frac{\pi mr}{R}\right)\cos\left(n\theta\right),\\
w_0 &= \sum_{m=1}^{\infty}\sum_{n=1}^{\infty}W(t)\sin\left(\frac{\pi mr}{R}\right)\sin\left(n\theta\right),
\end{aligned} \tag{24}$$

The parameters m and n correspond to the wave numbers in the radial and azimuthal directions, with both indices spanning the positive integer domain (1, 2, ...). Substituting Eq. (24) into Eqs. (18)-(22), one can obtain

$$\sum_{m=1}^{M}\sum_{n=1}^{N}\left(\mathbf{I}\cdot\begin{bmatrix}\frac{\partial^2U(t)}{\partial t^2}\\ \frac{\partial^2V(t)}{\partial t^2}\\ \frac{\partial^2W(t)}{\partial t^2}\\ \frac{\partial^2\Phi_r(t)}{\partial t^2}\\ \frac{\partial^2\Phi_\theta(t)}{\partial t^2}\end{bmatrix}+\varsigma\cdot\begin{bmatrix}U(t)\\ V(t)\\ W(t)\\ \Phi_r(t)\\ \Phi_\theta(t)\\ W(t)^2\\ W(t)^3\\ U(t)\cdot W(t)\\ V(t)\cdot W(t)\\ \Phi_r(t)\cdot W(t)\\ \Phi_\theta(t)\cdot W(t)\end{bmatrix}+\Xi\cdot\begin{bmatrix}\frac{\partial U(t)}{\partial t}\\ \frac{\partial V(t)}{\partial t}\\ \frac{\partial W(t)}{\partial t}\\ \frac{\partial\Phi_r(t)}{\partial t}\\ \frac{\partial\Phi_\theta(t)}{\partial t}\end{bmatrix}+\begin{bmatrix}0\\ 0\\ F_c(t)\delta\left(w_i-w\right)\\ 0\\ 0\end{bmatrix}\right)=0 \tag{25}$$

The Galerkin discretization isolates transverse displacement inertia within the resulting ordinary differential equations.

$$\sum_{m=1}^{M}\sum_{n=1}^{N}\left(\mathbf{M}\cdot\begin{bmatrix}\frac{\partial^2U(t)}{\partial t^2}\\ \frac{\partial^2V(t)}{\partial t^2}\\ \frac{\partial^2W(t)}{\partial t^2}\\ \frac{\partial^2\Phi_r(t)}{\partial t^2}\\ \frac{\partial^2\Phi_\theta(t)}{\partial t^2}\end{bmatrix}+\mathbf{K}\cdot\begin{bmatrix}U(t)\\ V(t)\\ W(t)\\ \Phi_r(t)\\ \Phi_\theta(t)\\ W(t)^2\\ W(t)^3\\ U(t)\cdot W(t)\\ V(t)\cdot W(t)\\ \Phi_r(t)\cdot W(t)\\ \Phi_\theta(t)\cdot W(t)\end{bmatrix}+\mathbf{C}\cdot\begin{bmatrix}0\\ 0\\ \frac{\partial W(t)}{\partial t}\\ 0\\ 0\end{bmatrix}+\begin{bmatrix}0\\ 0\\ \mathbf{F}\\ 0\\ 0\end{bmatrix}\right)=0 \tag{26}$$

Here, **[M]**, **[K]**, and **[C]** respectively represent the mass, stiffness, and damping matrices, and $\mathbf{F}=\iint_A F_c(t)\delta\left(w_s-w\right)\cdot\sin\left(\frac{m\pi}{\ell}r\right)\sin\left(n\theta\right)dA$. In the end, Runge-Kutta method is employed to solve Eq. (26).

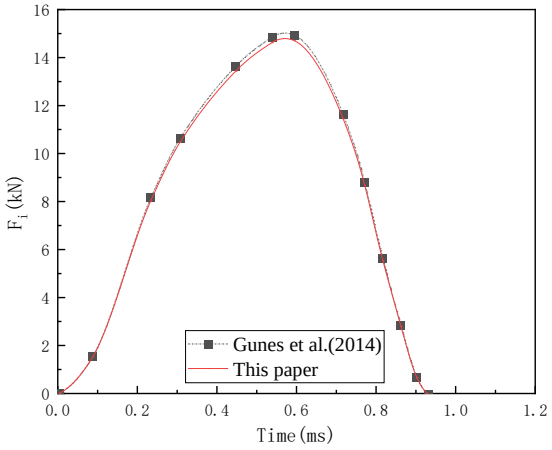

Fig. 2 Comparative analysis of contact force time histories (Ω=0): Present findings vs. Gunes *et al.* (2014)

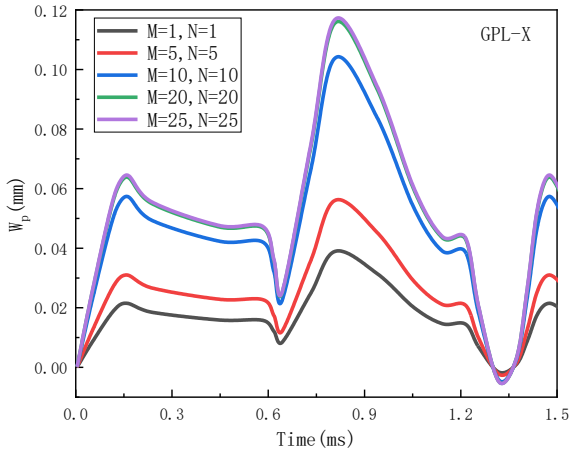

Fig. 3 Convergence verification (GPL-X, Porosity-III, e_1=0.3, w_{GPL}=0.1%, Ω=200 rad/s)

4. Numerical analysis

Due to the fact that the spinning circular plates under low-velocity impact remain unstudied. For validation, while the low-velocity impact behavior of FG-GPL porous structures remains unexplored, this study validates its methodology by replicating the functionally graded circular plate impact test from Gunes *et al.* (2014). Key parameters—adapted in our MATLAB code—include plate properties and the impactor are the same as Gunes *et al.* (2014), as depicted in Fig. 2, our FSDT-based results align closely with Gunes' 3D elasticity solution, exhibiting a maximum discrepancy of <2%.

In the following part, during the calculation: For the circular plate: Radius R=0.75 m, h=0.1 m, E_m=130 GPa, v_m=0.34, ρ_m=8960 kg/m³, For the GPL reinforcement:E_{GPL}=1.01 TPa, ρ_{GPL}= 1062.5 kg/m³, v_{GPL}=0.186, w_{GPL}=1.5 μm, l_{GPL}=2.5 μm, t_{GPL}=15 nm; For the spherical impactor (ball): R_s=0.05 m, E_s=210 GPa, ρ_s=7850 kg/m³, v_s=0.3; Impact velocity V=5 m/s.

Numerical reliability necessitates convergence verification. Fig. 3 demonstrates time-history

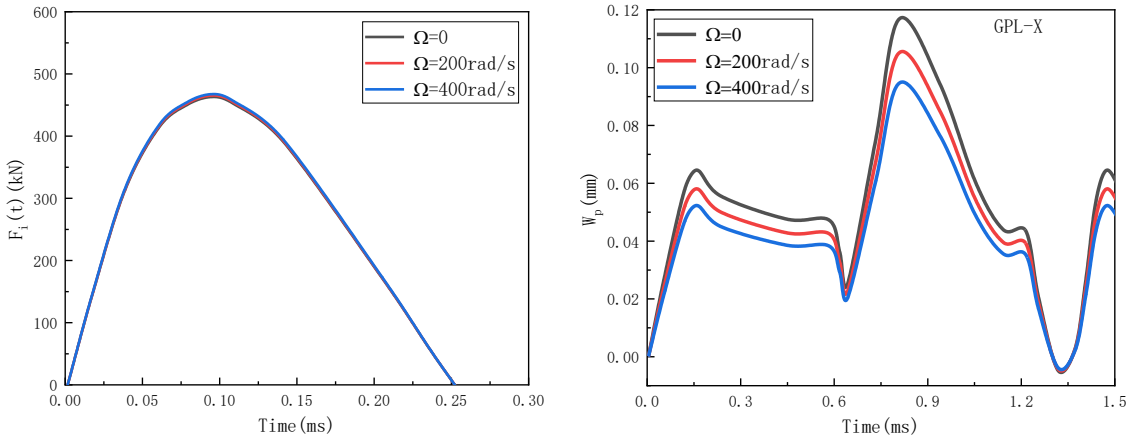

Fig. 4 Effect of spinning velocity (GPL-X, Porosity-III, e_1=0.3, w_{GPL}=0.1%)

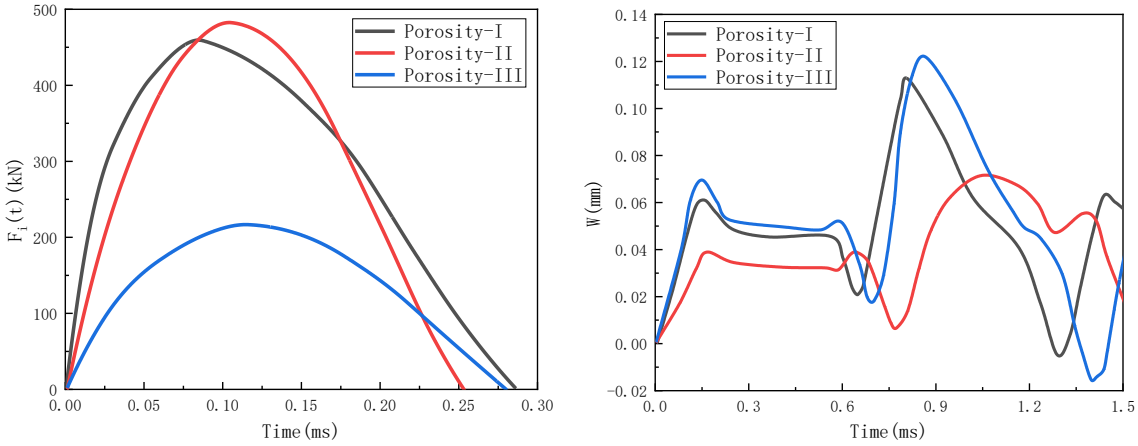

Fig. 5 Effect of porosity distribution (GPL-X, e_1=0.2, w_{GPL}=0.1%, Ω=200 rad/s)

convergence for the circular plate's nonlinear transient dynamics under uniform blast load. Solutions stabilize at M=N=20, subsequently adopted as the computational standard.

Fig. 4 systematically investigates the influence of spinning velocity (Ω) on contact force and displacement dynamics. Quantitative analysis reveals two markedly distinct trends: contact force magnitude exhibits negligible variation (fluctuation<2.7% within Ω=0-400 rad/s), while contact displacement demonstrates significant rotational speed dependence, decreasing from 0.11734 mm to 0.0948 mm as rotational speed increases from 0 to 400 rad/s, with maximum displacement occurring at t=0.095 ms when the plate reaches peak deformation. Mechanistic interpretation: this divergence originates from rotational hardening effects. Centrifugally induced circumferential stress fields constrain structural deformation while exerting minimal influence on local contact mechanics governed by graphene dispersion morphology. The stabilizing centrifugal potential suppresses displacement-amplifying vibration modes, yet remains subordinate to contact stiffness within load transmission pathways.

Fig. 5 reveals distinct patterns in contact behavior across different porosity distributions. Porosity-II demonstrates the highest contact force among the tested configurations, while Porosity-

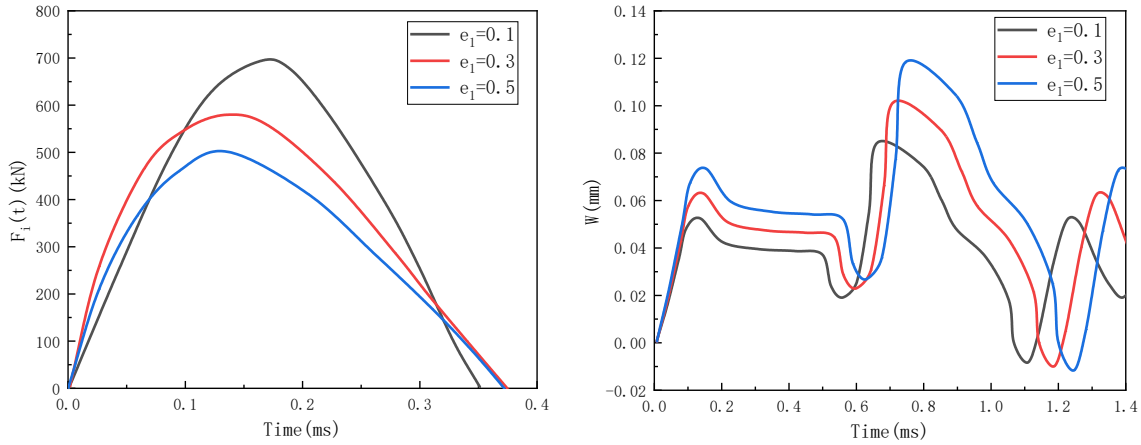

Fig. 6 Effect of porosity coefficient (GPL-X, Porosity-I, w_{GPL}=0.1%, Ω=200 rad/s)

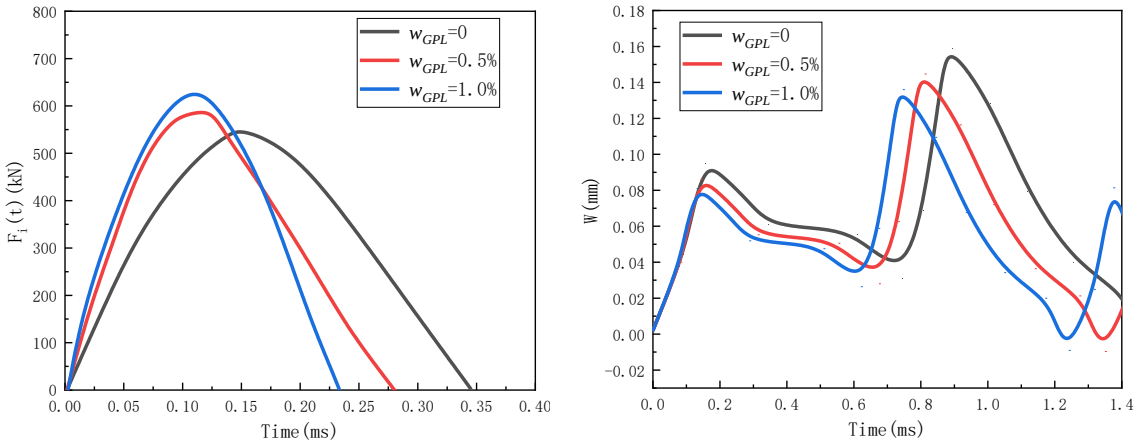

Fig. 7 Effect of porosity coefficient (GPL-X, Porosity-I, e_1=0.5, Ω=200 rad/s)

III shows the lowest contact force magnitude. Conversely, Porosity-II exhibits the smallest contact displacement, with Porosity-III presenting the most significant displacement response. These observations suggest an inverse relationship between porosity concentration and mechanical resistance, where increased porosity correlates with reduced load-bearing capacity and greater deformation under applied forces.

Fig. 6 shows that the porosity coefficient e_1 significantly affects the contact behavior between materials. As e_1 increases, the contact force generally decreases due to reduced effective contact area and load-bearing capacity. Meanwhile, the contact displacement also shows a decreasing trend with higher e_1 values, as the porous structure provides more compliance and energy absorption capacity. This inverse relationship occurs because greater porosity creates more internal voids and weaker structural integrity, leading to lower resistance to deformation. The combined effects demonstrate how material porosity influences mechanical interactions, where both contact force and displacement diminish with increasing e_1, reflecting the compromised structural stiffness and altered deformation characteristics of porous materials.

Fig. 7 depicts that the mass fraction w_{GPL} of graphene platelets plays a crucial role in

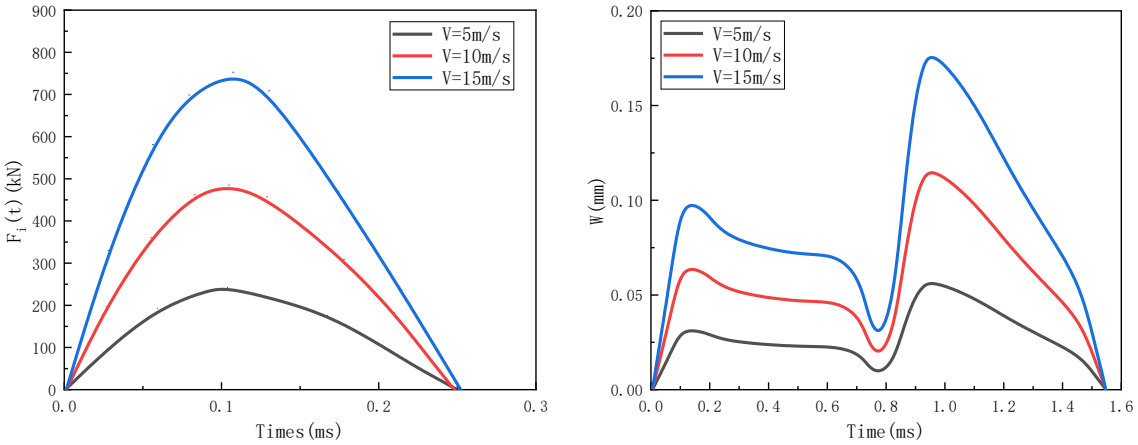

Fig. 8 Effect of impact velocity *V*(GPL-X, Porosity-I, e_1=0.2, w_{GPL}=0.1%, Ω=200 rad/s)

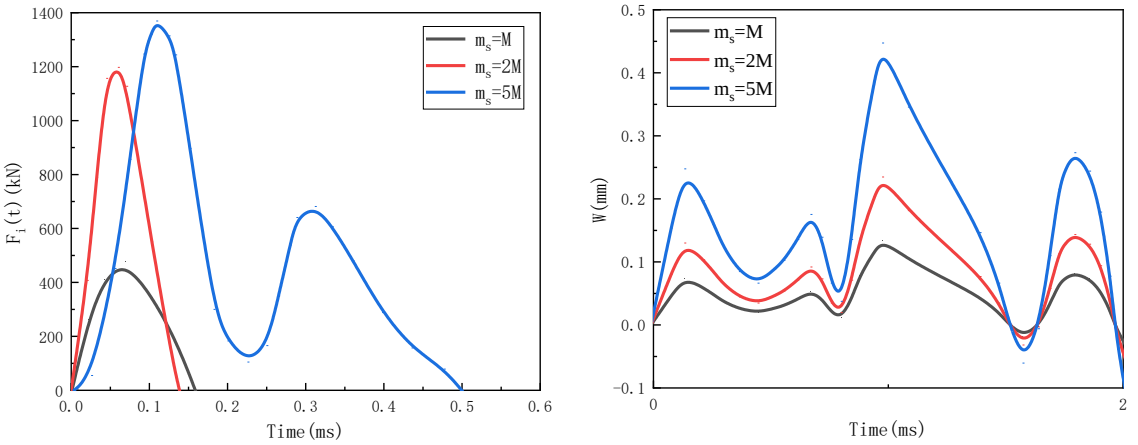

Fig. 9 Effect of impactor mass m_s (GPL-X, Porosity-III, e_1=0.2, w_{GPL}=0.1%, Ω=200 rad/s)

determining the contact behavior of composite materials. As w_{GPL} increases, the contact force generally rises due to enhanced stiffness and load-bearing capacity from the reinforcing graphene platelets. Conversely, the contact displacement tends to decrease with higher w_{GPL}, as the improved structural integrity restricts deformation. This dual effect arises because graphene reinforcement strengthens the material matrix, increasing resistance to external forces while reducing flexibility. The observed trends highlight how graphene content modulates mechanical interactions, where greater w_{GPL} leads to higher contact forces but smaller displacements, reflecting the trade-off between reinforcement and deformation characteristics.

Fig. 8 shows that the impact velocity *V* significantly influences the dynamic contact behavior between colliding bodies. As *V* increases, both the contact force and displacement exhibit a rising trend. Higher impact velocities generate greater kinetic energy, leading to intensified force transmission at the contact interface. Simultaneously, the enhanced energy input causes more pronounced material deformation, resulting in larger contact displacements. This correlated growth occurs because faster impacts induce stronger stress waves and inertial effects, which collectively amplify the mechanical response. The observed pattern demonstrates how impact velocity governs

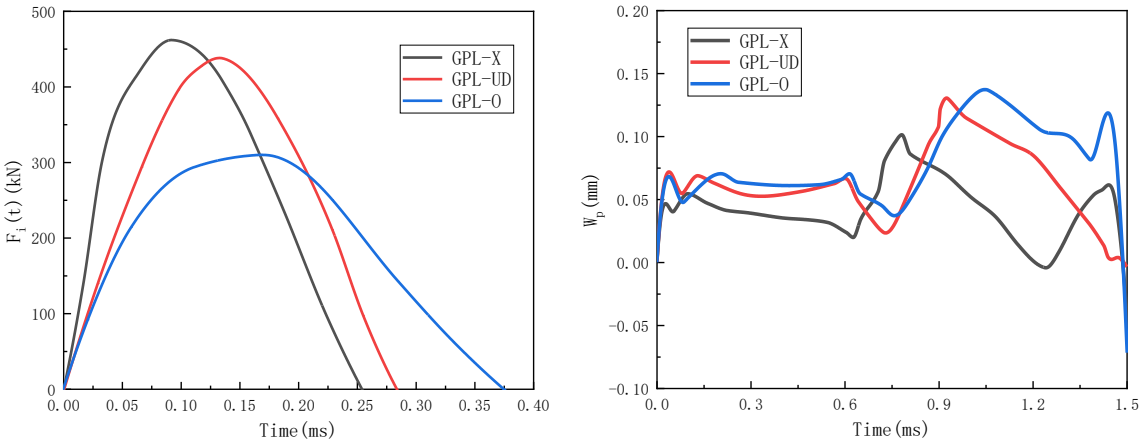

Fig. 10 Effect of GPLs distributions (Porosity-III, e_1=0.3, w_{GPL}=0.1%, Ω=200 rad/s)

collision dynamics, where elevated V values simultaneously escalate contact forces and displacements, reflecting the energy-dependent nature of impact interactions.

Fig. 9 shows the influence of impactor mass (m_s) on contact behavior reveals complex dynamic interactions. As m_s increases from M to 5M, the contact force exhibits progressive intensification with a notable transition: while m_s=M or 2M produces single-peak force profiles, the m_s=5M case develops dual-peak characteristics. This bifurcation likely arises from stress wave reflections within the impactor and target material, where higher mass enables sequential energy release phases. Concurrently, contact displacement amplifies with growing m_s due to enhanced momentum conservation and prolonged contact duration. The dual-peak phenomenon specifically suggests inertial dominance at critical mass ratios, where initial impact energy partitions into primary compression and secondary rebound phases. Larger displacements correlate with deeper material indentation, as increased kinetic energy at higher m_s overcomes structural resistance more effectively. These observations highlight mass-dependent energy redistribution mechanisms, where wave propagation timing and inertial delays jointly sculpt the force-displacement relationship, particularly manifesting in the distinctive dual-peak signature at m_s=5M.

Fig. 10 shows that under the impact of the striker ball, the GPL-X distribution pattern exhibits the highest contact force magnitude, while the GPL-O distribution pattern yields the lowest contact force magnitude. Conversely, the GPL-X pattern demonstrates the smallest impact-induced displacement, whereas the GPL-O pattern results in the largest contact displacement.

5. Conclusions

This study investigates the dynamic contact behavior of nanocomposite plates under coupled physical fields, focusing on four key variables: graphene platelet (GPL) distribution patterns, rotational velocity, porosity architectures, and impactor mass. The research reveals that GPL spatial configuration fundamentally alters material stiffness characteristics, while rotational effects induce selective hardening that modifies global displacement without affecting local contact forces. Porosity distribution is shown to create distinct tradeoffs between mechanical resistance and energy absorption. Most notably, a critical mass threshold triggers a dynamic regime shift in

contact behavior, manifested through dual-peak force profiles resulting from stress wave interference phenomena. These findings collectively demonstrate how multi-scale material design and external loading conditions synergistically govern impact resistance mechanisms.

(1) GPL distribution patterns determine load transfer efficiency, with X-type configurations exhibiting superior stiffness enhancement compared to O-type arrangements.

(2) Rotational hardening provides a unique mechanism for controlling structural displacement independently of contact force characteristics.

(3) Porosity architectures create predictable performance tradeoffs between mechanical resistance and energy dissipation capacity.

(4) Impactor mass governs contact dynamics through inertial effects, with higher masses inducing sequential energy release phases.

(5) The emergence of dual-peak force profiles beyond a critical mass ratio indicates stress wave dominance in energy partitioning.

Acknowledgement

The funding Natural Science Foundation of Hunan Province(2024JJ8109), Scientific research project of Hunan Provincial Department of Education (24B0974 and 22B0956), and Xiangtan science and technology planning project (CG-YB20240004) are appreciated.

Reference

Abo, Z.F., Jweeg, M.J., Njim, E.K., Mouthanna, A., Flayyih, J.A., Madan, R., Khobragade, P. and Rai, P.K. (2025), "Nonlinear frequency and dynamic response of PLA polymeric imperfect FG sandwich plates under hygrothermal conditions", *Couple. Syst. Mech.*, **14**(1), 1-19. https://doi.org/10.12989/csm.2025.14.1.001.

Bui, T.T., Vu, M.D., Pham, N.N., Cao, V.D. and Vu, H.N. (2024), "Nonlinear thermo-mechanical dynamic buckling and vibration of FG-GPLRC circular plates and shallow spherical shells resting on the nonlinear viscoelastic foundation", *Arch. Appl. Mech.*, **94**(12), 3715-3729. https://doi.org/10.1007/s00419-024-02691-6.

Caglar, H., Caglar, A., Ataei, A., Salmani, R. and Efkar, A. (2025), "Post-buckling behavior of lattice core sandwich cylindrical shell with functionally graded graphene platelets reinforced face layer resting on elastic foundation", *Adv. Nano Res.*, **18**(1), 83-95. https://doi.org/10.12989/anr.2025.18.1.083.

Cheng, Y.H. and She, G.L. (2025), "Nonlinear dynamics of rotating graphene-reinforced composite blades under 1:2 internal resonance in fluid-submerged environments", *Ocean Eng.*, **341**(4), 122717. https://doi.org/10.1016/j.oceaneng.2025.122717.

Cheng, Y.H., She, G.L., Eltaher, M.A. (2025), "Nonlinear internal resonance of graphene-reinforced metal foam plates with initial geometric imperfection under non-uniform temperature field", *Aerosp. Sci. Technol.*, **165**, 110491. https://doi.org/10.1016/j.ast.2025.110491.

Dai, H.L., Guo, Z.Y. and Yang, L. (2014), "Nonlinear dynamic response of functionally graded materials circular plates subject to low-velocity impact", *J. Compos. Mater.*, **47**(22), 2797-2807. https://doi.org/10.1177/0021998312458132.

Fan, Y.H. and She, G.L. (2026), "Low-velocity impact response of rotating 2D-FGM annular plates with variable thickness", *Commun. Nonlin. Sci. Numer. Simul.*, **152**(Part D), 109373. https://doi.org/10.1016/j.cnsns.2025.109373.

Fan, Y.H., She, G.L. and Eltaher, M. A. (2025a), "Nonlinear vibrations of two-directional functionally

graded spinning annular plates with variable thickness", *Thin Wall. Struct.*, **216**(A), 113627. https://doi.org/10.1016/j.tws.2025.113627.

Fan, Y.H., She, G.L. and Li, C. (2025b), "Nonlinear transient response analysis of revolution doubly curved shells", *Arch. Civil Mech. Eng.*, **25**(3), 145. https://doi.org/10.1007/s43452-025-01187-6.

Gunes, R., Aydin, M., Apalak, M.K. and Reddy, J.N. (2011), "The elasto-plastic impact analysis of functionally graded circular plates under low-velocities", *Compos. Struct.*, **93**(2), 860-869. https://doi.org/10.1016/j.compstruct.2010.07.008.

Gunes, R., Aydin, M., Apalak, M.K. and Reddy, J.N. (2014), "Experimental and numerical investigations of low velocity impact on functionally graded circular plates", *Compos. Part B: Eng.*, **59**, 21-32. https://doi.org/10.1016/j.compositesb.2013.11.022.

Hu, Y.D. and Li, W.Q. (2018), "Study on primary resonance and bifurcation of a conductive circular plate rotating in air-magnetic fields", *Nonlin. Dyn.*, **93**(2), 671-687. https://doi.org/10.1007/s11071-018-4217-y.

Hu, Y.D. and Li, W.Q. (2019), "Magnetoelastic axisymmetric multi-modal resonance and Hopf bifurcation of a rotating circular plate under aerodynamic load", *Nonlin. Dyn.*, **97**(2), 1295-1311. https://doi.org/10.1007/s11071-019-05049-8.

Hu, Y.D. and Ma, B.B. (2019), "Magnetoelastic combined resonance and stability analysis of a ferromagnetic circular plate in alternating magnetic field", *Appl. Math. Mech. (English Ed.)*, **40**(7), 925-942. https://doi.org/10.1007/s10483-019-2496-7.

Hu, Y.D. and Wang, T. (2015), "Nonlinear resonance of the rotating circular plate under static loads in magnetic field", *Chin. J. Mech. Eng.*, **28**(6), 1277-1284. https://doi.org/10.3901/CJME.2015.0720.097.

Hu, Y.D. and Wang, T. (2016), "Nonlinear free vibration of a rotating circular plate under the static load in magnetic field", *Nonlin. Dyn.*, **85**(3), 1825-1835. https://doi.org/10.1007/s11071-016-2798-x.

Hu, Y.D. and Xu, H.R. (2021), "Nonlinear natural vibration of a circular plate in the non-uniform induced magnetic field", *Arch. Appl. Mech.*, **91**(6), 2513-2533. https://doi.org/10.1007/s00419-021-01901-9.

Hu, Y.D., Li, Z., Du, G.J. and Wang, Y.N. (2018), "Magneto-elastic combination resonance of rotating circular plate with varying speed under alternating load", *Int. J. Struct. Stab. Dyn.*, **18**(3), 1850032. https://doi.org/10.1142/S0219455418500323.

Jafary, H., Attariani, H. and Golmakani, M.E. (2025), "Non-linear thermoelastic analysis of circular sandwich porous plates reinforced with functionally graded graphene platelets", *Proc. Inst. Mech. Eng., Part C-J. Mech. Eng. Sci.*, **239**(10), 3809-3827. https://doi.org/10.1177/09544062241312580.

Kalhori, A., Bayat, M.J. and Asemi, K. (2023a), "Buckling analysis of stiffened functionally graded multilayer graphene platelet reinforced composite plate with circular cutout embedded on elastic support subjected to in-plane normal and shear loads", *Result. Eng.*, **20**, 101563. https://doi.org/10.1016/j.rineng.2023.101563.

Kalhori, A., Bayat, M.J. and Asemi, K. (2023b), "Buckling response of functionally graded multilayer graphene platelet-reinforced composite plates with circular/elliptical cutouts supporting on an elastic foundation under normal and shear loads", *Front. Mech. Eng.*, **9**, 1293713. https://doi.org/10.3389/fmech.2023.1293713.

Khatounabadi, M., Jafari, M. and Asemi, K. (2025), "Low-velocity impact analysis of functionally graded porous circular plate reinforced with graphene platelets", *Wave. Random Complex Media*, **35**(4), 7838-7864. https://doi.org/10.1080/17455030.2022.2091182.

Kumar, R., Miglani, A. and Kumar, R. (2024), "Axisymmetric deformation of thick circular plate in microelongated thermoelastic solid", *Couple. Syst. Mech.*, **13**(3), 231-245. https://doi.org/10.12989/csm.2024.13.3.231.

Lahdiri, A., Hadji, L., Atmane, H.A. and Kadri, M. (2024), "Isogeometric finite element method for the dynamic analysis of functionally graded plates", *Couple. Syst. Mech.*, **13**(6), 509-527. https://doi.org/10.12989/csm.2024.13.6.509.

Li, L.F., Wang, X.Z. and Zhou, Y.H. (2011), "Dynamic characteristics of traveling waves for a rotating laminated circular plate with viscoelastic core layer", *J. Sound Vib.*, **330**(12), 2836-2847. https://doi.org/10.1016/j.jsv.2011.01.011.

Li, W.Q. and Hu, Y.D. (2021), "Magneto-aeroelastic internal resonances of a rotating circular plate based on

gyroscopic systems decoupling", *Int. J. Struct. Stab. Dyn.*, **21**(1), 2150010. https://doi.org/10.1142/S0219455421500103.

Li, W.Q., Hu, Y.D. and Li, Z. (2024), "Magneto-aero-elastic superharmonic and subharmonic resonances, bifurcations and chaos of conductive spinning circular plates", *Int. J. Bifurcat. Chaos*, **33**(01), 2330001. https://doi.org/10.1142/S021812742330001X.

Li, Z., Hu, Y.D. and Li, J. (2017), "Magnetoelastic principal parametric resonance of a rotating electroconductive circular plate", *Shock Vib.*, **2017**, 5196847. https://doi.org/10.1155/2017/5196847.

Ma, Z.S., She, G.L. and Li, C. (2025), "Nonlinear thermal flutter analysis of graphene platelets reinforced metal foam arbitrary quadrilateral plates", *Arch. Civil Mech. Eng.*, **25**(4), 203. https://doi.org/10.1007/s43452-025-01262-y.

Mars, J., Ben, S.L., Wali, M. and Dammak, F. (2018), "Elasto-plastic modeling of low-velocity impact on functionally graded circular plates", *Int. J. Appl. Mech.*, **10**(4), 1850038. https://doi.org/10.1142/S1758825118500382.

Mirdrikvandi, G., Loghman, A., Arani, A.G. and Maraghi, Z.K. (2025), "Semi-analytical method for vibration of asymmetric rotating circular annular sandwich plate with porous core and CNTRC face sheets", *Arch. Civil Mech. Eng.*, **25**(4), 227. https://doi.org/10.1007/s43452-025-01270-y.

Morozov, N.F., Lukin, A.V. and Popov, I.A. (2024), "Gyroscopically coupled in-plane and out-of-plane vibrations of rotating hollow circular plate: Case of in-plane axis of rotation", *Vestnik St. Petersburg Univ., Math.*, **57**(2), 241-253. https://doi.org/10.1134/S1063454124700092.

Nam, V.H., Tu, B.T., Doan, C.V., Nam, P.N. and Duc, V.M. (2025), "A new semi-analytical approach for nonlinear dynamic responses of functionally graded porous graphene platelet-reinforced circular plates and spherical shells", *Proc. Inst. Mech. Eng., Part C-J. Mech. Eng. Sci.*, **239**(3), 730-742. https://doi.org/10.1177/09544062241282766.

Nguyen, T.P., Dang, T.D., Bui, T.T., Vu, M.D., Le-Nguyen, K., Pham, T.H. and Vu, H.N. (2024), "Nonlinear thermo-mechanical axisymmetric stability of FG-GPLRC spherical shells and circular plates resting on nonlinear elastic medium", *Ship. Offshore Struct.*, **19**(6), 820-830. https://doi.org/10.1080/17445302.2023.2214489.

Raissi, H. (2021), "Dynamic damage analysis of a ten-layer circular composite plate subjected to low-velocity impact", *Arch. Civil Mech. Eng.*, **21**(3), 96. https://doi.org/10.1007/s43452-021-00238-y.

Shariyat, M. and Jafari, R. (2013a), "A micromechanical approach for semi-analytical low-velocity impact analysis of a bidirectional functionally graded circular plate resting on an elastic foundation", *Meccanica*, **48**(9), 2127-2148. https://doi.org/10.1007/s11012-013-9729-4.

Shariyat, M. and Jafari, R. (2013b), "Nonlinear low-velocity impact response analysis of a radially preloaded two-directional-functionally graded circular plate: A refined contact stiffness approach", *Compos. Part B: Eng.*, **45**(1), 981-994. https://doi.org/10.1016/j.compositesb.2012.05.014.

She, G.L. and He, Y.J. (2025), "Nonlinear 1: 1 internal resonance in graphene platelet-reinforced fluid-conveying pipes", *Appl. Math. Mech. (English Ed.)*, **46**(10), 1903-1920. https://doi.org/10.1007/s10483-025-3305-8.

Shen, X.Q., Li, T., Xu, L., Kiarasi, F., Babaei, M. and Asemi, K. (2024), "Free vibration analysis of FG porous spherical cap reinforced by graphene platelet resting on Winkler foundation", *Adv. Nano Res.*, **16**(1), 11-26. https://doi.org/10.12989/anr.2024.16.1.011.

Song, M.T., Li, X.Q., Kitipornchai, S., Bi, Q.S. and Yang, J. (2019), "Low-velocity impact response of geometrically nonlinear functionally graded graphene platelet-reinforced nanocomposite plates", *Nonlin. Dyn.*, **95**(3), 2333-2352. https://doi.org/10.1007/s11071-018-4695-y.

Vu, H.N., Nguyen, V.T., Pham, N.N., Tran, Q.M. and Vu, M.D. (2025a), "Nonlinear vibration responses of GPL-reinforced circular plates and spherical shells stiffened by multi-step spiderweb stiffeners with piezoelectric layer", *Ship. Offshore Struct.*, 1-19. https://doi.org/10.1080/17445302.2025.2537944.

Vu, H.N., Pham, N.N., Bui, T.T., Vu, M.D. and Nguyen, T.P. (2025b), "A new semi-analytical approach for nonlinear electro-thermo-mechanical dynamic responses of FG-GPLRC shallow spherical caps and circular plates with porous core", *J. Thermoplast. Compos. Mater.*, **38**(3), 911-932. https://doi.org/10.1177/08927057241259760.

Wang, X., Guo, X.F., Babaei, M., Fili, R. and Farahani, H. (2023), "Natural frequency analysis of joined conical-cylindrical-conical shells made of graphene platelet reinforced composite resting on Winkler elastic foundation", *Adv. Nano Res.*, **15**(4), 367-384. https://doi.org/10.12989/anr.2023.15.4.367.

Wu, X.J. (2023), "Nonlinear finite element vibration analysis of functionally graded nanocomposite spherical shells reinforced with graphene platelets", *Adv. Nano Res.*, **15**(2), 141-153. https://doi.org/10.12989/anr.2023.15.2.141.

Xia, L.Q., Wang, R.Q., Chen, G., Asemi, K. and Tounsi, A. (2023), "The finite element method for dynamics of FG porous truncated conical panels reinforced with graphene platelets based on the 3-D elasticity", *Adv. Nano Res.*, **14**(4), 375-389. https://doi.org/10.12989/anr.2023.14.4.375.

Yang, F.L., Wang, Y.Q. and Liu, Y.F. (2022), "Low-velocity impact response of axially moving functionally graded graphene platelet reinforced metal foam plates", Aerospace Science and Technology, **123**, 107496. https://doi.org/10.1016/j.ast.2022.107496.

Yang, Y.Q., Wang, Z.M. and Wang, Y.Q. (2019), "Thermoelastic coupling vibration and stability analysis of rotating circular plate in friction clutch", *J. Low Freq. Noise Vib. Act. Control*, **38**(2), 558-573. https://doi.org/10.1177/1461348418817465.

Younesian, D., Aleghafourian, M.H. and Esmailzadeh, E. (2015), "Vibration analysis of circular annular plates subjected to peripheral rotating transverse loads", *J. Vib. Control*, **21**(7), 1443-1455. https://doi.org/10.1177/1077546313499178.

Zhang, J.H. and Zhou, Q. (2025), "Numerical investigation of nonlinear stability of functionally graded circular plates reinforced by graphene platelets", *Mech. Compos. Mater.*, **61**(3), 455-472. https://doi.org/10.1007/s11029-025-10286-7.

Zhang, J.H., Cao, C.X. and Ma, L.S. (2024), "Modeling and solving for vibration and buckling of circular functionally graded dielectric plates reinforced by graphene platelets considering complex conditions", *Eng. Res. Expr.*, **6**(1), 015087. https://doi.org/10.1088/2631-8695/ad2578.

Zhang, Y.W., She, G.L. and Eltaher, M.A. (2023), "Nonlinear transient response of graphene platelets reinforced metal foams annular plate considering rotating motion and initial geometric imperfection", *Aerosp. Sci. Technol.*, **142**(B), 108693. https://doi.org/10.1016/j.ast.2023.108693.

Zhao, B. and She, G.L. (2025), "Vibration analysis of graphene reinforced metal foam coupled plates under arbitrary boundary and coupled conditions", *Eng. Struct.*, **343**(C), 121143. https://doi.org/10.1016/j.engstruct.2025.121143.

Zhao, B., Eltaher, M.A. and She, G.L. (2025), "Dynamic response analysis of acoustic black hole plates with cutouts under arbitrary boundary constraints", *Thin Wall. Struct.*, **217**(Part A), 113859. https://doi.org/10.1016/j.tws.2025.113859.

Zhou, Q., Zhang, J.H., Zhao, Y.G. (2024), "Nonlinear buckling and postbuckling of circular plates reinforced with graphene platelets using the shooting method", *Int. J. Struct. Stab. Dyn.*, **24**(01), 2450001. https://doi.org/10.1142/S0219455424500019.

Zohra, A., Rabia, B. and Tahar, H.D. (2024), "Study and analysis of porosity distribution effects on the buckling behavior of functionally graded plates subjected to diverse thermal loading", *Couple. Syst. Mech.*, **13**(2), 115-132. https://doi.org/10.12989/csm.2024.13.2.115.